Geophys. J. Int. (2009) **179,** 1055–1070 doi: 10.1111/j.1365-246X.2009.04319.x

Tidal triggering of earthquakes in the Northeast Pacific Ocean

William S. D. Wilcock

School of Oceanography, University of Washington, Box 357940, *Seattle,* WA 98195-7940, *USA. E-mail: wilcock@u.ocean.washington*

Accepted 2009 July 2. Received 2009 June 16; in original form 2008 September 7

SUMMARY

There have been many searches for evidence of tidal triggering in earthquake catalogues. With the exception of volcanically active regions, the more rigorous studies in continental settings tend to find no correlation or only a very weak correlation. In the oceans, the effect of loading by the ocean tides can increase tidal stresses by about an order of magnitude over continental settings. In recent years, several studies have reported evidence of tidal triggering in oceanic regions and such observations can represent a useful constraint on models of earthquake rupture. In this paper, I systematically search for a link between ocean tide height and the incidence of earthquakes in the Northeast Pacific Ocean, a region of high-amplitude open ocean tides. The focal mechanisms of most of the earthquakes in these catalogues are unknown but it can be shown that tidal stresses will in most instances promote failure at low tides. I investigate three declustered data sets comprising (1) earthquakes from 1980 to 2007 on the Juan de Fuca plate and in the Queen Charlotte Fault region from land based catalogues; (2) earthquakes from 1992 to 2001 on the Juan de Fuca plate located with the US Navy's Sound Surveillance System (SOSUS) hydrophone array and (3) earthquakes from 1980 to 2001 south of Alaska and the Aleutians located with land based networks. I look at the distributions of earthquakes with ocean tide phase, height, and tidal range and apply Schuster and binomial tests and Monte Carlo simulations to determine if they deviate significantly from random. The results show no evidence of triggering during intervals of increased tidal range but all three data sets show a significant increase in earthquake incidence at low tides. The signal is particularly strong in the land-based catalogue for the Juan de Fuca Plate and Queen Charlotte Fault regions where there is a 15 per cent increase in the rate of seismicity within 15° of the lowest tides. The signal is weakest in the SOSUS data set, which may reflect the lower average tidal range at epicentres in this data set or an analysis that is influenced by gaps in the catalogue. The triggering signal in the Alaska/Aleutian may be partially obscured by earthquakes in the Aleutians where the total tidal stresses can be significantly out of phase with the ocean tide height. The increase in the rates of seismicity I observe at low tides is less than observed by local networks on mid-ocean ridges, similar to the prediction from an analysis of global thrust earthquakes and greater than inferred by extrapolating laboratory simulations of fault failure under tidal loading.

Key words: Earthquake interaction, forecasting, and prediction; Pacific Ocean.

INTRODUCTION

For more than a century scientists have searched for temporal correlations between the origin times of earthquakes and tidal stresses (e.g. Cotton 1922; Emter 1997). Although the amplitudes of tidal stresses are small compared to the stress drops that accompany earthquakes (Kanamori & Anderson 1975), the rates at which tidal stresses change are generally significantly higher than average rates a which tectonic stresses build up (Emter 1997). For a simple Coulomb threshold model for failure, earthquakes should occur preferentially at times of favourable tidal stress.

Studies in continental settings report mixed results, although a careful review shows that many studies reporting positive correlations suffer from a lack of statistical rigor (Emter 1997). With the exception of local earthquakes in volcanically active regions (e.g. McNutt & Beavan 1981) careful studies show either no correlation or a weak correlation. For example, Vidale *et al.* (1998) analyse over 13000 declustered earthquakes occurring near the San Andreas and Calaveras faults. They find that the rate of earthquakes is slightly higher when the stress favours rupture but that the difference is not statistically significant at the 95 per cent confidence level. Wein & Shearer (2004) find no correlation with tides in a data set of 430 000

Southern California earthquakes. Recently, Métivier *et al.* (2009) report a correlation that is significant at the 99 per cent confidence level between solid earth tides and a data set of 442 000 global earthquakes.

The reason for a lack of a strong correlation in many data sets can be attributed to the long duration of earthquake nucleation relative to the tidal periods (Knopoff 1964; Dieterich 1987). Lockner & Beeler (1999) present a systematic set of laboratory experiments that confirm this explanation. Quantitative extrapolations of their results to the San Andreas predict that about 1 per cent of earthquakes should be correlated with tides (Lockner & Beeler 1999) and that $\sim 10^5$–10^6 earthquakes would be required to demonstrate a statistically robust correlation (Beeler & Lockner 2003). The interpretation of these results also suggests that a 10-fold increase in tidal stress amplitudes will lead to a 100-fold decrease in the number of events necessary to detect a correlation (Beeler & Lockner 2003).

In the open oceans and along continental margins, the loading effects of ocean tides can lead to tidal stresses that are up to an order of magnitude larger that the solid earth tides that dominate in continental interiors (Melchior 1983). Several earlier studies reported evidence for tidal triggering in oceanic regions (Berg 1966; Klein 1976). Over the past decade or so, the topic has received renewed interest as a result of more extensive earthquake catalogues and the recognition that the quantification of weak tidal triggering signals can contribute to the understanding of earthquake nucleation and static and dynamic earthquake triggering (e.g. Cochran *et al.* 2004).

Tsuruoka *et al.* (1995) applied a new algorithm to compute ocean loading stresses to a study of 1000 earthquakes of magnitude ≥ 6 in the Harvard centroid moment tensor (CMT) catalogue and found a significant increase in earthquakes at times of maximum tensile cubic stress for a subset of 75 normal faulting earthquakes located primarily on mid-ocean ridges. This study was criticized for the practice of over subdividing the data set in search of a positive correlation (Emter 1997). In a follow up study of 9350 globally distributed earthquakes of magnitude 5.5 or larger in the Harvard CMT catalogue, Tanaka *et al.* (2002a) report a correlation between the tidal phase of the shear stress resolved on reverse faults which is particularly strong for shallower and smaller earthquakes. They also find a weaker correlation for the phase of shallow and larger normal faulting events. Cochran *et al.* (2004) re-analysed the same data set taking into account the amplitude of the tidal stress. For the tidal normal stresses, they find a significant correlation for earthquakes at sites where the peak tidal stress amplitudes are in the top percentile. The correlation is particularly strong for reverse faults near coastlines where the fault plane has a shallow dip. In such settings earthquakes are favoured at low tide because the decrease in weight of the water column acts to unclamp the fault. Seventeen of the top 20 events and 25 of the next 40 occur during times of encouraging stress.

Two regional studies of temporal patterns of tidal triggering for shallow reverse faults in subduction zones suggest that tidal triggering is detectable and increases in strength over an interval of a few years prior to large earthquakes and disappears afterwards (Tanaka *et al.* 2002b, 2006). Studies of local earthquakes on the Juan de Fuca (Wilcock 2001; Tolstoy *et al.* 2002) and East Pacific Rise (Stroup *et al.* 2007) report particularly strong evidence for tidal triggering.

DATA SETS

In this study, I search for a correlation between earthquakes and tidal height in the Northeast Pacific Ocean using three catalogues of regional offshore earthquakes (Table 1). The first (Fig. 1a), hereafter termed the 'JdF/QCF' data set, covers the Juan de Fuca Plate and Queen Charlotte Fault regions and was obtained by merging hypocentres from the Advanced National Seismic System (ANSS) composite earthquake catalogue and the Canadian National Earthquake Database (CNED). I include earthquakes for the time interval 1980–2007 in a region defined by adjoining areas extending from 39 to 53°N and 225 to 237°E and from 53 to 57.5°N and 222 to 230°E. I exclude earthquakes that are <10 km offshore and earthquakes that have focal depths greater than 33 km or half the distance to the coast. In addition, I exclude all earthquakes in Hecate Strait and Queen Charlotte Sound. To eliminated duplicate earthquakes, I assume that the same earthquake is reported in both catalogues if the origin times differ by <30 s and the epicentres are <100 km apart. I keep the CNED solution if the epicentre in that catalogue lies within the Canadian Exclusive Economic Zone and the ANSS solution otherwise.

Table 1. Summary of earthquake data sets.

Region	Juan de Fuca Plate/ Queen Charlotte Fault	Juan de Fuca Plate	Offshore South of Alaska/ Aleutians Islands		JdF/QCF and A/AI
Abbreviated Name	JdF/QCF	SOSUS	A/AI	A/AI subset	Combined
Source Catalogues	ANSS, CNED	NOAA-PMEL	ANSS, AEIC	ANSS, AEIC	
Years	1980–2007	1992–2001	1980–2007	1980–2007	1980–2007
Latitude limits (°N)	39–53, 53–57.5	39–53	48–62	48–62[a]	
Longitude limits (°E)	225–237, 222–230	225–237	160–220	∼200–220[a]	
Number	12398	21644	14522	3569	26920
Size threshold	$M \geq 2$	$A_S \geq 200$ dB	$M \geq 2$	$M \geq 2$	$M \geq 2$
Number exceeding threshold	10209	20462	12387	3092	22596
Number declustered	5656	5290	5816	2000	11472
Mean latitude (°N)	46.6	44.6	54.4	57.7	50.5
Mean rms tide height (m)	0.74	0.66	0.63	0.87	0.68
Median rms tide height (m)	0.79	0.64	0.58	0.89	0.65
Mean tide range (m)	3.56	3.18	3.06	4.18	3.31
Mean flood fraction	0.506	0.505	0.528	0.506	0.517

Notes: AEIC, Alaska Earthquake Information Center Earthquake Database; ANSS, Advanced National Seismic System composite Earthquake catalogue; CNED, Canadian National Earthquake Database, NOAA-PMEL, National Oceanic and Atmospheric Administration-Pacific Marine Environmental Laboratory. The final five rows apply to the declustered data sets and list the mean latitude of the earthquakes, the mean and median rms tide height, the mean tide range and the mean fraction of the time the tidal height is increasing at the earthquake locations.

[a]The data set A/AI subset was obtained by including only earthquakes from the region with rms tide heights exceeding 0.65 m (see Fig. 2).

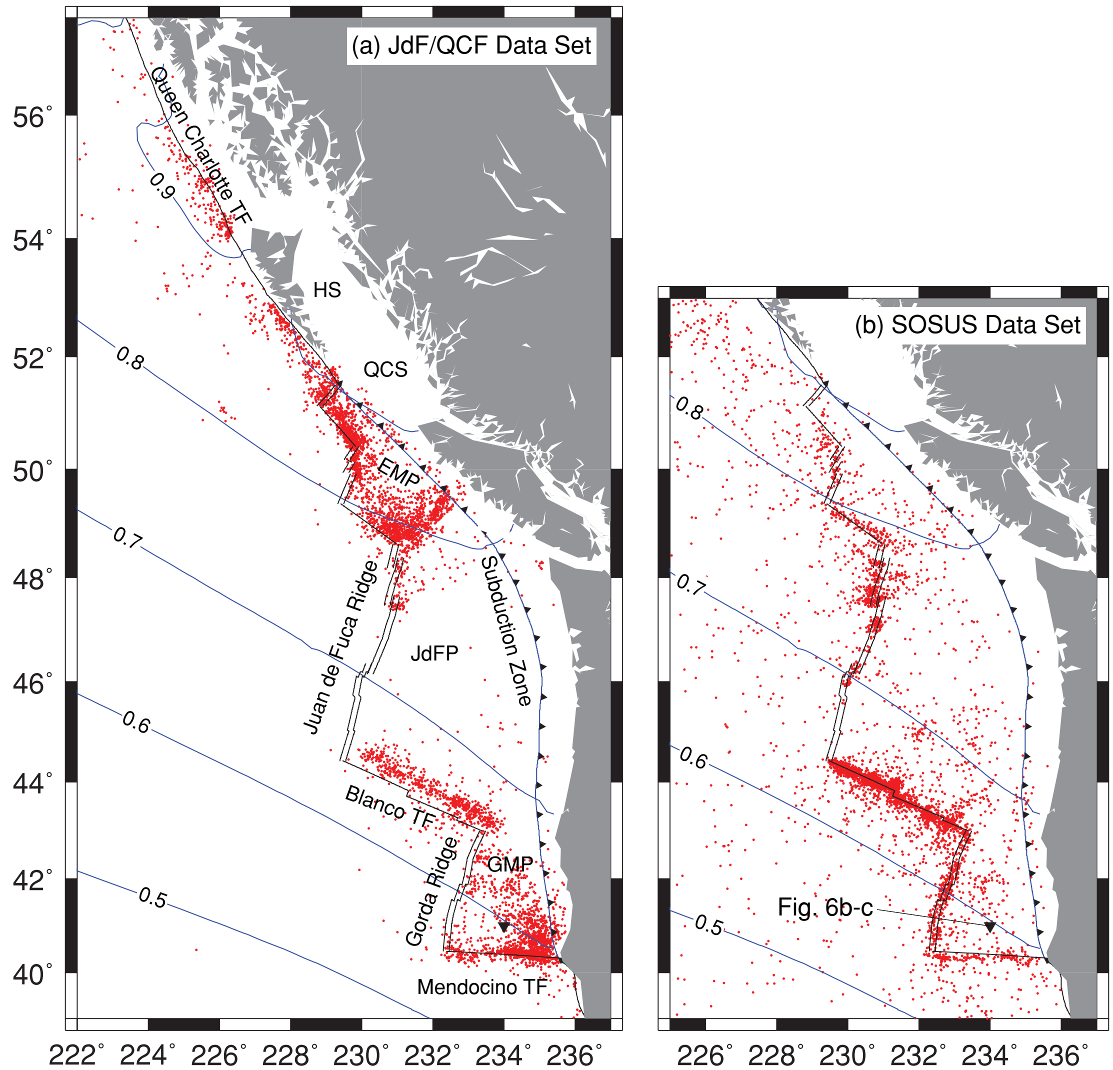

Figure 1. (a) Map of the Juan de Fuca Plate and Queen Charlotte fault regions showing the location of land (grey shading), labelled plate boundaries (single black lines for transform faults, double black lines for oceanic spreading centres and a saw tooth line for subduction faults); contours of the root mean square tide height (blue feint lines labelled in units of meters); and the location of offshore epicentres (red dots) for the 'JdF/QCF' data set. The epicentres were obtained by merging the Advanced National Seismic System composite earthquake catalogue and the Canadian National Earthquake Database for 1980–2007 and then applying a declustering algorithm (see text for more details). Abbreviations are as follows: EMP Explorer microplate; HS, Hecate Strait; GMP, Gorda microplate; JdFP, Juan de Fuca Plate; QCS, Queen Charlotte Sound; TF, transform fault. (b) As for (a) except the map is limited to the Juan de Fuca plate region and the epicentres are from the 'SOSUS' data set. The epicentres are for 1992–2001 and were obtained by applying a declustering algorithm to the NOAA/PMEL catalogue of epicentres obtained from T-phases recorded on the US Navy's 'SOSUS' hydrophone arrays. A labelled inverted triangle shows the location of the tidal stresses plotted in Figs 6(b) and (c).

The second data set (Fig. 1b), hereafter termed SOSUS, comprises epicentres in the Juan de Fuca Plate region that have been determined by the National Oceanic and Atmospheric Administration's Pacific Marine Environmental Laboratory with T-phase data from the US Navy's Sound Surveillance System (SOSUS) hydrophone array (Fox *et al.* 1994). Earthquake locations from this classified array are only available from mid-1991 and the on-line catalogue is incomplete after 2002 May. I include earthquakes for the time interval 1992–2001 in a region extending from 39 to 53°N and 225 to 237°E. Hypocentral depths are not determined from the T-phase data and so I include all epicentres that are >20 km offshore.

The third data set (Fig. 2), hereafter termed 'A/AI', covers the Pacific Ocean south of Alaska and the Aleutian Islands and was constructed by merging earthquakes from ANSS catalogue and the Alaska Earthquake Information Center (AEIC) earthquake database. I selected earthquakes for the time interval 1980–2007 in a region extending from 48 to 62°N and 165°E to 220°W. I use the same criteria to eliminate near shore and deep earthquakes as for the 'JdF/QCF' data set and also exclude all earthquakes in Prince William Sound, Cook Inlet and Shelikof Strait and as well as those earthquakes north of the Alaskan Peninsula and Aleutian Island chain. I use the same criteria as for the 'JdF/QCF' data set to identify duplicate earthquakes and for such events assume the solution from the ANSS catalogue.

Fig. 3 shows plots of the cumulative earthquake count exceeding a variable magnitude or source pressure amplitude in the case of the 'SOSUS' data set. From the change in slope of these curves it appears the data sets are only complete at magnitudes above ∼4 and ∼4.5 for the 'JdF/QCF' and 'A/AI' data sets, respectively, and

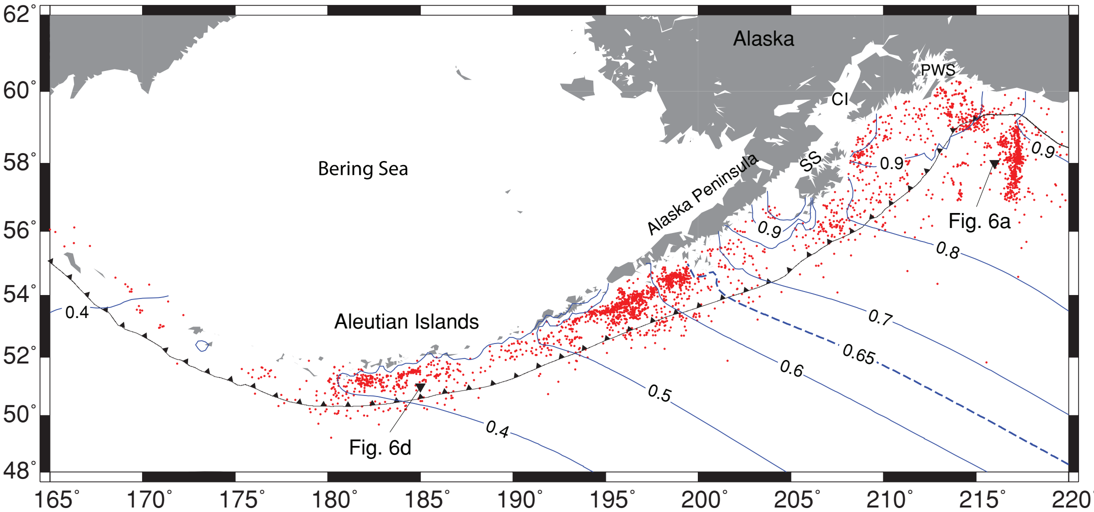

Figure 2. Map of offshore southern Alaska and the Aleutian Islands plotted using the same conventions as Fig. 1 showing offshore epicentres for 1980–2007 for the 'A/AI' data set constructed by merging ANSS catalogue and the Alaska Earthquake Information Center earthquake database and then applying a declustering algorithm (see text). A dashed contour for rms tide heights of 0.65 m shows the threshold used to create a 'A/AI' data subset of earthquakes at locations with large tidal ranges. Inverted triangles show the locations of the tidal stresses plotted in Figs 6(a) and (d). Abbreviations are as follows: CI, Cook Inlet; PWS, Prince William Sound; SS Shelikof Strait.

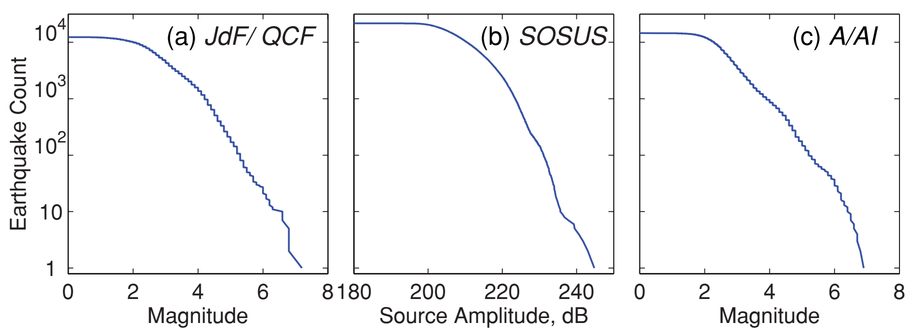

Figure 3. (a) Plot of the cumulative count of earthquakes exceeding a variable threshold magnitude for the 'JdF/QCF' data set of earthquakes offshore of the Pacific Northwest recorded by land networks. The plot was made before applying a declustering algorithm. (b) As for (a) except the 'SOSUS' data set is used and the plot is for source amplitude instead of magnitude. (c) As for (a) except for the 'A/AI' data set of earthquakes to the south of Alaska and the Aleutian Islands recorded by land networks.

for a source pressure amplitudes above 225 dB [which corresponds approximately to a magnitude of 2.75 (Schreiner *et al.* 1995)] for the 'SOSUS' data set. The numbers of earthquakes that exceed these size thresholds are too small to resolve a weak correlation with tides and so I chose to limit my analysis to incomplete data sets with magnitude $M \geq 2$ for the land network and source pressure amplitudes $A_S \geq 200$ dB ($M \geq \sim 1.5$) for the 'SOSUS' data set. These thresholds only reduce the size of the full data sets slightly (Table 1).

Any statistical search for temporal correlations in an earthquake catalogue will be biased by the presence of earthquake swarms. In order to minimize this effect, I apply the declustering algorithm of Reasenberg (1985) to eliminate all earthquakes that fall within a temporal and spatial interaction zone of an earlier earthquake. The temporal interaction zone is defined as the interval necessary to wait in order to have a 95 per cent probability of observing the next event in the sequence assuming the rate of aftershock is given by Omari's Law. I set lower and upper bounds for this interval to 2 and 10 d, respectively. The horizontal spatial interaction zone of earthquake is modelled by estimating the source dimension from the magnitude and multiplying it by a factor of 10. For all but the largest earthquakes, the epicentral uncertainties are likely to be much larger than the estimated dimension of the interaction zone. Therefore, I reduce the distance between two earthquakes by the sum of their estimated location errors before determining whether the second earthquake lies within the interaction zone of the first. For the 'SOSUS' data set, I assume the maximum 2σ epicentral errors listed in the catalogue. For the land networks, the catalogues do not always include an estimate of the location error and there may also be non-systematic location biases in catalogues constructed by merging locations from multiple networks. I therefore assume an epicentral error for all earthquakes of $(10 + 0.1x)$ km where x is the distance offshore. These epicentral errors, as well as the choice of the declustering parameters, are clearly somewhat arbitrary but I have explored more relaxed and stringent choices and find that they do not change the primary results of this study. The final declustered data sets used for the tidal triggering analysis each comprise between 5000 and 6000 earthquakes (Table 1) whose epicentres are plotted in Figs 1 and 2.

Although the 'JdF/QCF' data set completely overlaps the spatial and temporal bounds of the 'SOSUS' data set, there are only 208 events in common out of 1903 earthquakes in the 'JdF/QCF'

Table 2. Comparison of distribution of earthquakes in the two data sets that cover the Juan de Fuca Plate.

	JdF/QCF			SOSUS		
	N_{reg}	N_{reg}/N_{tot}	$\bar{h}_q$ (cm)	N_{reg}	N_{reg}/N_{tot}	$\bar{h}_q$ (cm)
Mendocino TF	829	0.15	−3.1	186	0.04	6.7
Blanco TF	616	0.11	−4.8	2611	0.49	−2.6
Queen Charlotte TF	594	0.11	−0.1	–		
Gorda ridge	136	0.02	−2.7	425	0.08	−1.1
Juan de Fuca ridge	134	0.02	−7.8	527	0.10	−0.7
Subduction zone	171	0.03	−0.5	46	0.01	2.7
Gorda MP	713	0.13	0.0	119	0.02	2.5
Explorer MP	2232	0.39	−1.7	351	0.07	−0.5
Other	231	0.04	−4.5	1025	0.19	0.2
All	5656		−2.1	5290		−1.1

Notes: Notation is as listed in the notation section. MP, microplate; TF, transform fault. To assign earthquakes to a geographic region we used the present day plate boundaries from the PLATES project (Coffin *et al.* 1998) and assign an earthquake to a transform fault or ridge if it is closest to and within 50 km of the plate boundary. Earthquakes are assigned to the subduction zone if they are east of the plate boundary; to the Gorda microplate if they are on the microplate and more than 50 km from a ridge or transform plate boundary; and to the Explorer microplate if they are on the microplate.

data set that lie within the temporal and spatial bounds of the 'SOSUS' data set. The distribution of events in the two data sets (Fig. 1, Table 2) is substantially different. The 'SOSUS' array has a substantially lower detection threshold well offshore particularly towards the southern end of the Juan de Fuca Plate but is less sensitive to events near the continental shelf and slope. Nearly half the events in the 'SOSUS' data set lie on the Blanco transform fault compared with only 11 per cent for the 'JdF/QCF' data set (Table 1). The proportion of events on the Gorda and Juan de Fuca Ridges is also much higher in the 'SOSUS' data set. Conversely, nearly half the epicentres for the 'JdF/QCF' data set are located relatively near shore on the Explorer and Gorda microplates compared with 9 per cent for the 'SOSUS' data set. Another effect that contributes to the small number of events in common, is that some large earthquakes are missing from the 'SOSUS' catalogue because the T-phases saturate the hydrophone records which prevents the automatic location procedure from determining the azimuth to the event (Robert Dziak 2008, personal communication).

With the exception of a large number of earthquakes near 217°E in the vicinity of two M 7.6 intraplate events in 1987 and 1988 most of the earthquakes in the 'A/AI' data set lie to the north of the subduction zone plate boundary (Fig. 2). Given the depth selection criteria, most of these events must be located in the North American plate. There are large concentrations of earthquakes near 195–200°E and 181–186°E and relatively few earthquakes west of 180°E. To a large extent these variations mirror the proximity of seismic stations (Taber *et al.* 1991).

Because the catalogues are incomplete at the minimum magnitudes considered, it is important to be aware of annual, seasonal and daily biases in the catalogues that may arise from variations in network sensitivity. The number of earthquakes per year (Figs 4a–c) varies substantially in each data set and at least partially reflects changes in network geometry. In particular, the large increase in the number of earthquakes in final few years of the 'A/AI' data set is a result of expanded monitoring of volcanoes (Brantley *et al.* 2004). All three data sets (Figs 4d–f) and in particular, the 'SOSUS' data set (Fig. 4e) show apparent seasonal biases with more earthquakes in the summer months. There is a notable daily signal in the 'JdF/QCF' (Fig. 4g) and 'A/AI' (Fig. 4i) data sets with fewer earthquakes from 12:00 to 24:00 GMT and 16:00 to 24:00 GMT, respectively. These intervals of reduced earthquake rates coincide approximately with the working day and could be a result of diurnal variations in either anthropogenic or meteorological noise; the latter being perhaps more likely in the sparsely populated Alaska and Aleutian Island region.

EXPECTED CORRELATIONS WITH TIDE HEIGHT

The tidal stresses at any location beneath the oceans result from two sources; direct loading from ocean tides and solid earth tides. If the fault orientation and slip direction are known the tidal shear, normal and Coulomb stresses promoting failure on the fault can be estimated using models of the Earth's tides. This approach has been used as the basis for tidal triggering studies of both the global Harvard CMT catalogue (Tsuruoka *et al.* 1995; Tanaka *et al.* 2002a; Cochran *et al.* 2004) and regional studies of earthquakes on major faults (Vidale *et al.* 1998; Tanaka *et al.* 2002b; Tanaka *et al.* 2006). In the Northeast Pacific Ocean, there are a relatively small number of fault plane solutions (Braunmiller & Nábělek 2002; Ristau *et al.* 2003; Braunmiller & Nábělek 2008; Tréhu *et al.* 2008) and so a statistically robust analysis for tidal triggering must either make assumptions about the orientation of fault planes and slip directions or just search for correlations with tide height.

For the 'JdF/QCF' and 'SOSUS' data sets, it is possible to make reasonable assumptions about the dominant faulting style in many regions. For examples earthquakes on the Blanco Transform Fault are right-lateral strike-slip, earthquakes on the Gorda and Juan de Fuca Ridge are normal faulting with ridge-perpendicular extension, and earthquakes on the Explorer plate are dominantly strike-slip with north-south pressure axes (Kreemer *et al.* 1998). However, the focal mechanisms of a significant number of smaller earthquakes in these regions may deviate from the regional norm; for example ∼20 per cent of the focal mechanisms presented by Braunmiller & Nábělek (2008) for the Blanco transform fault are normal mechanisms resulting from pull-apart basins. In other areas, such as the Sovanco transform fault (Cowan *et al.* 1986) and the ridge-transform intersections (e.g. Rowlett & Forsyth 1984; Cessaro & Hussong 1986), the patterns of faulting are likely quite complex.

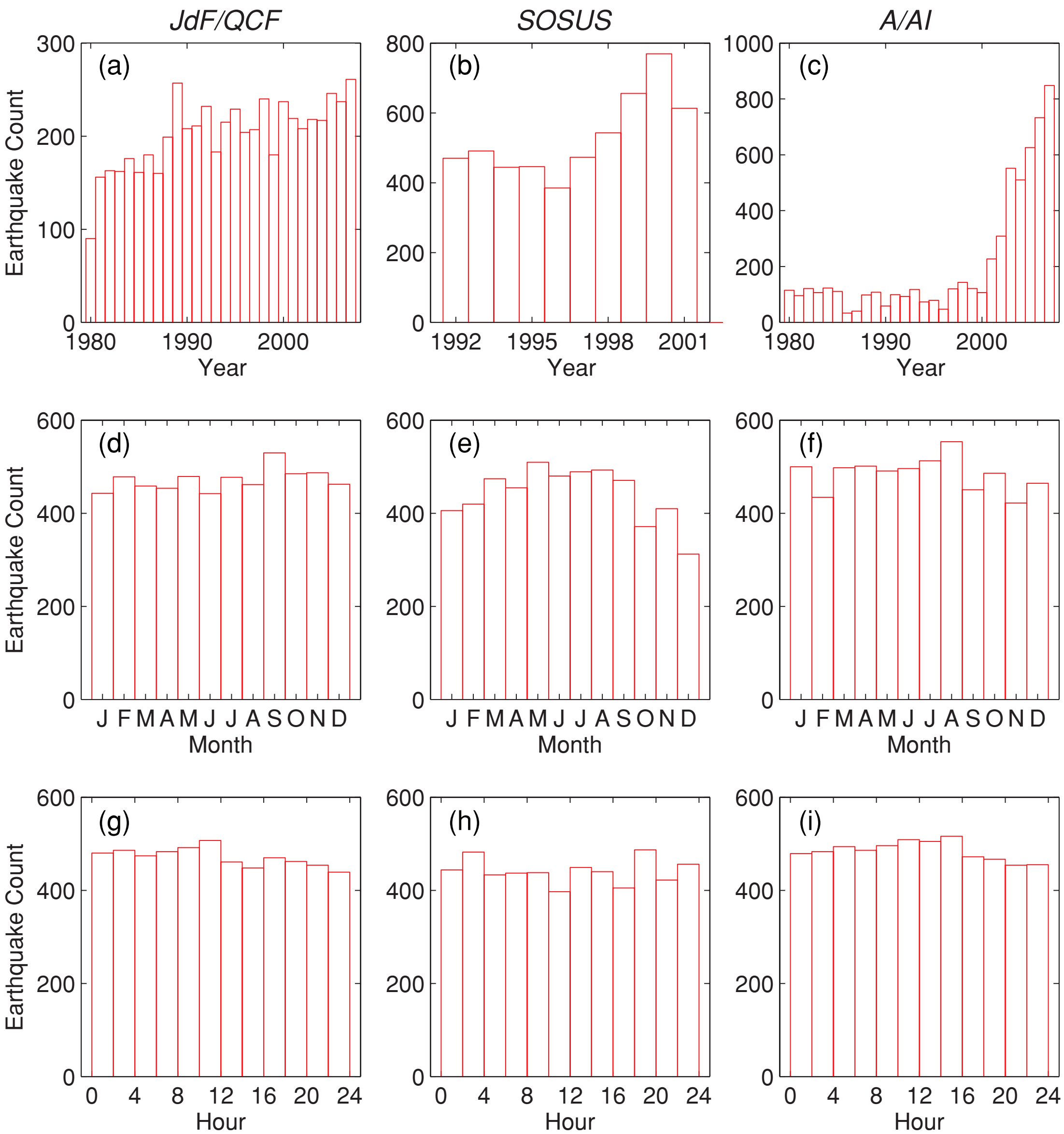

Figure 4. (a) Histogram of the earthquake count in each year for the 'JdF/QCF' data set. (b) and (c) As for (a) except for the 'SOSUS' and 'A/AI' data sets, respectively. (d)–(f) As for (a)–(c) except the histograms show the earthquake count in each month of the year adjusted to account for the lengths of months. (g)–(i) As for (a)–(c) except the histograms show the earthquake count as a function of the hour of the day (times are Universal Time).

For the 'A/AI' data set, it is much harder to assign the faulting style. There are relatively few focal mechanisms solutions available for offshore earthquakes and the state of stress in the forearc may transition from margin-normal tension to compression as one moves away from the trench and the stresses are also influenced by the curvature of the arc (Wang & He 1999; Kelin Wang 2004, personal communication). Because of all these uncertainties, I choose to limit my investigation of each data set to a search for correlations with tidal height.

The vertical stress perturbation, $\Delta\sigma_{zz}$ just below the seafloor that results from loading by ocean tides is

$$\Delta\sigma_{zz} = \rho g h, \tag{1}$$

where ρ is the density of seawater, g is the acceleration of gravity and h the height of the tide relative to its mean value. In this study, I use the TPXO7.1 global model (Egbert *et al.* 1994; Egbert & Erofeeva 2002) to estimate ocean tides. I assume that eq. (1) also approximates the perturbation to the vertical principal stress at the depth of shallow earthquakes. I estimate the horizontal stresses, $\Delta\sigma_{xx}$ and $\Delta\sigma_{yy}$ from tidal loading assuming uniaxial strain (e.g. Turcotte & Schubert 2002)

$$\Delta\sigma_{xx} = \Delta\sigma_{yy} = \frac{\nu}{1-\nu}\Delta\sigma_{zz}, \tag{2}$$

where ν is Poisson's ratio. The tidal perturbations to the normal stress, $\Delta\sigma_n$ and shear stress, $\Delta\tau$ acting on a fault (e.g. Jaeger & Cook 1979) with dip δ and a rake λ (the angle between the fault strike and the slip direction with the sign convention chosen so that positive values correspond to uplift of the hanging wall) are given by

$$\Delta\sigma_n = \Delta\sigma_{zz}\left(\cos^2\delta + \frac{\nu}{1-\nu}\sin^2\delta\right)$$
$$\Delta\tau = \Delta\sigma_{zz}\frac{2\nu-1}{1-\nu}\sin\delta\ \cos\delta\ \sin\lambda. \tag{3}$$

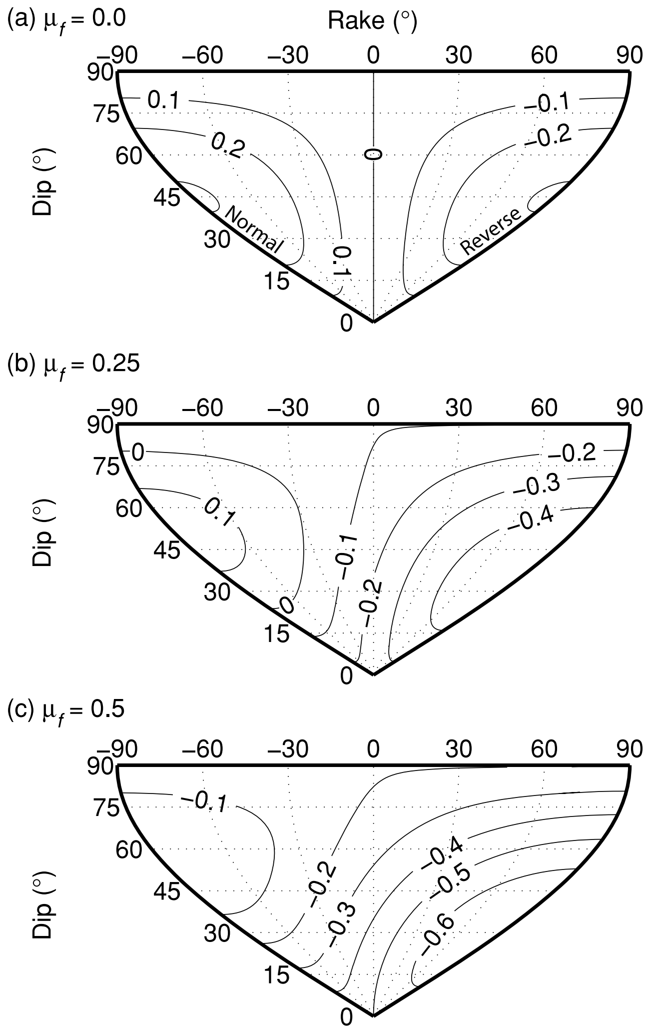

Figure 5. Tidal Coulomb stress calculated using eqs (3) and (4) normalized to the vertical tidal loading stress as a function of fault rake and dip for an effective coefficient of friction (a) $\mu_f = 0.0$, (b) $\mu_f = 0.25$ and (c) $\mu_f = 0.50$. For this plot the rake is defined as the angle between the fault strike and slip direction of the footwall with positive angles for an slip upwards; the strike is chosen so that the magnitude of the rake is $\leq 90°$. Thus, the left side of the plot corresponds to pure normal faulting, the right side to reverse faulting and the centre of the top axis to a vertical strike-slip fault. The plot shape has been chose so that if the orientation of fault orientations and slip directions were uniformly distributed they would have equal density on the plot. The sign convention is such that positive values indicate an increase in Coulomb stress at high tide.

The Coulomb stress is a measure of the total stress promoting failure and the contribution to this from tidal loading is defined (e.g. Scholtz 2002)

$$\Delta\sigma_c = \Delta\tau - \mu_f \Delta\sigma_n. \tag{4}$$

where μ_f is an effective coefficient of friction that takes into account pore pressure. In principal, the value of μ_f can vary from 0.0 to 0.8 (e.g. King *et al.* 1994). Fig. 5 shows the Coulomb stress from ocean tidal loading normalized to $\Delta\sigma_{zz}$ as a function of the fault dip and rake for three choices of μ_f assuming a Poisson's ratio of 0.28 (Shaw 1994). The sign convention is chosen such that a positive value of the Coulomb stress indicates that ocean loading will favour fault motions at high tide while a negative value indicates that fault motions are favoured at low tide. When $\mu_f = 0$ (Fig. 5a), ocean loading promotes failure on normal faults at high tides and reverse faults at low tide with no effect on strike-slip faults. However, since the normal compressive stresses in all directions are smallest at low tide, the effect of increasing μ_f is to increase the range of fault orientations on which failure is promoted at low tides (Figs 5b and c). For $\mu_f \geq 0.5$ (Fig. 5c), ocean loading promotes failure on all faults at low tide. Thus, unless a fault population is dominated by normal faults or the effective coefficient of friction is very small, tidal loading should tend to promote failure at low tides.

A number of investigators have estimated μ_f and the reported values vary significantly. Studies of the distribution aftershocks following California earthquakes concluded that they were consistent with any value of μ_f between 0.0 and 0.6 (King *et al.* 1994; Deng & Sykes 1997). Spatial and temporal changes in the rate of regional seismicity or aftershocks are interpreted in terms of low values of 0.1–0.3 (Reasenberg & Simpson 1992) and 0.2 (Gross & Bürgmann 1998) for the 1989 Loma Prieta earthquake and a high value of 0.6 for the 1992 Landers earthquake (Gross & Kisslinger 1997). Kagen & Jackson (1998) look at global and Southern Californian earthquake catalogues and conclude that there is no systematic concentration of aftershocks in the dilatational quadrants of large earthquakes, a result that requires $\mu_f < 0.2$. Numerical models of Alaskan neotectonics based on the observed fault slip rates, directions of most compressive horizontal stress and geodetic data yield a best for $\mu_f = 0.17$ (Bird 1996). Cochran *et al.* (2004) find that the highest correlation between the occurrence of thrust earthquakes and the strongest tides occurs for μ_f between 0.2 and 0.6. Thus, the preponderance of studies seem to favour values of μ_f that are low but significantly greater than zero. However, it is likely that that μ_f varies spatially and with the exception of Cochran *et al.* (2004) no values have been specifically obtained for oceanic regions.

Solid earth tides will not affect the vertical stress just below the seafloor but will lead to horizontal stress perturbation that can be estimated from the predicted horizontal tidal strains assuming plane stress (e.g. Jaeger & Cook 1979)

$$\begin{aligned}
\Delta\sigma_{xx} &= \frac{E}{1-\nu^2}\left(\Delta\varepsilon_{xx} + \nu\Delta\varepsilon_{yy}\right) \\
\Delta\sigma_{yy} &= \frac{E}{1-\nu^2}\left(\nu\Delta\varepsilon_{xx} + \Delta\varepsilon_{yy}\right) \\
\Delta\sigma_{xy} &= \frac{E}{1+\nu}\Delta\varepsilon_{xy}.
\end{aligned} \tag{5}$$

where E is Young's modulus, $\Delta\varepsilon_{xx}$ and $\Delta\varepsilon_{yy}$ are the horizontal tidal normal strains and $\Delta\varepsilon_{xy}$ and $\Delta\sigma_{xy}$ are the horizontal tidal shear strain and stress, respectively. I assume that these relationships hold down to the depth of shallow oceanic earthquakes and estimate the horizontal strains from solid earth tides using the SPOTL software (Agnew 1996, 1997).

The open ocean tides in the northeast Pacific are quite large and have root mean square (rms) amplitudes within the study areas that range from ~0.4 to 1.0 m (Figs 1 and 2). Taking $\rho = 1030$ kg m^{-3}, $g = 9.8$ m s^{-2} and $\nu = 0.28$, the equivalent rms tidal loading stresses are $\Delta\sigma_{zz} = 4000$–10000 Pa and $\Delta\sigma_{xx} = \Delta\sigma_{yy} = 1600-3900$ Pa. In the areas covered by this study the solid earth tides are not generally in phase with the ocean loading. The rms amplitudes decrease from north to south and assuming reasonable properties for the lower oceanic crust (a Young's modulus $E = 1.1 \times 10^{11}$ Pa; $\nu = 0.28$) vary from 1400 to 2000 kPa in the N–S direction and 1100 to 1250 kPa in the E–W direction. For the mantle properties ($E = 1.6 \times 10^{11}$ Pa, $\nu = 0.28$), these ranges increase to 2200 to 2900 and 1700 to 1900 Pa, respectively. Thus, the horizontal stresses from

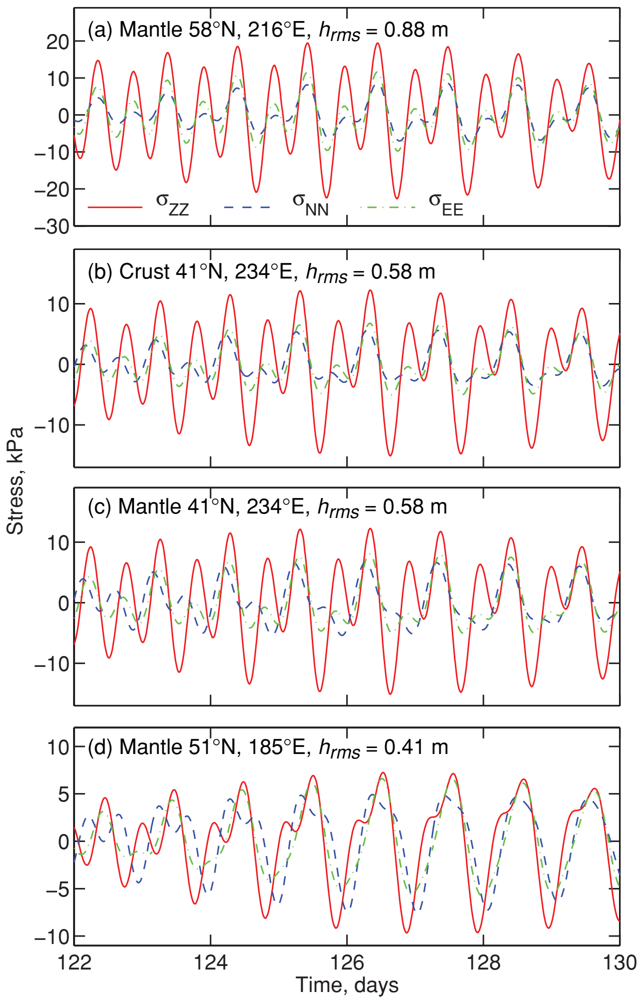

Figure 6. (a) Predicted vertical (red solid line) and north-south horizontal (blue dashed) and east–west horizontal (green dot–dashed) normal stresses due to the combined effects of ocean tide loading and solid-earth tides for a 8 day interval in 2000 (time in days is relative to the start of the year) for (a) the mantle at 58°N, 216°E; (b) the crust at 41°N, 234°E; (c) the mantle at 41°N, 234°E and (d) the mantle at 51°N, 185°. The sign convention is that compressive stresses are positive; the vertical stress is thus a scaled version of the tide height (eq. 1).

solid earth tides are generally somewhat smaller than those from ocean loading in the crust but fairly comparable in the mantle.

To assess the combined effects of ocean loading and solid earth tides I looked at the total tidal stresses at various locations in the study region. Fig. 6 shows the tidal stresses predicted for the crust at three representative sites (shown in Figs 1 and 2). In the northern Juan de Fuca plate region and offshore Alaska (Fig. 6a), the rms tide height exceeds ∼0.65 m and ocean loading dominates. All the tidal normal stresses are essentially in phase and the predicted ratio of the vertical to horizontal stress is close to that predicted by eq. (2). In the southern Juan de Fuca plate and offshore western Alaska Peninsula regions where the rms tide height varies from 0.5 to 0.65 m the vertical tidal normal stress lags the north–south stresses (Figs 6b and c). However except for cycles where the north–south horizontal stresses are small, the lag is generally $< \sim 1$ hr in the crust (Fig. 6b) and $< \sim 2$ hr in the mantle (Fig. 6c). Only in parts of the Aleutians where the rms tide height is <0.5 m are there substantial phase differences between the normal tidal stress components (Fig. 6d). These are particularly apparent for north–south stresses during intervals when the tidal range is small.

The median rms tide heights for the three data sets range from 0.58 to 0.79 (Table 1) and so for about half the earthquakes, the tidal stresses should be closely in phase with the tide height. For the remainder, the horizontal normal stresses may have significant phase lags particularly in the north–south direction. These may tend to weaken any observed correlation between earthquakes and tide height.

METHOD

Most studies of tidal triggering consider histograms of the phases of earthquake origin times in the tidal cycle and test for a non-random distribution using a Schuster test (e.g. Emter 1997). The probability, P_S that the phase distribution is non-random is approximated by

$$P_S = \exp\left(\frac{-R^2}{N_{\rm tot}}\right), \tag{6}$$

where $N_{\rm tot}$ is the number of earthquakes and R is the vector sum of the phasors

$$R^2 = \left(\sum_1^{N_{\rm tot}} \cos\phi\right)^2 + \left(\sum_1^{N_{\rm tot}} \sin\phi\right)^2. \tag{7}$$

The term ϕ is the earthquake phase and I define this as 0°/360° at high tide and 180° at low tide with linear interpolation in between (Fig. 7a). The tides in the Northeast Pacific are notably asymmetric particularly near the Aleutians with increasing (flood) tides up to

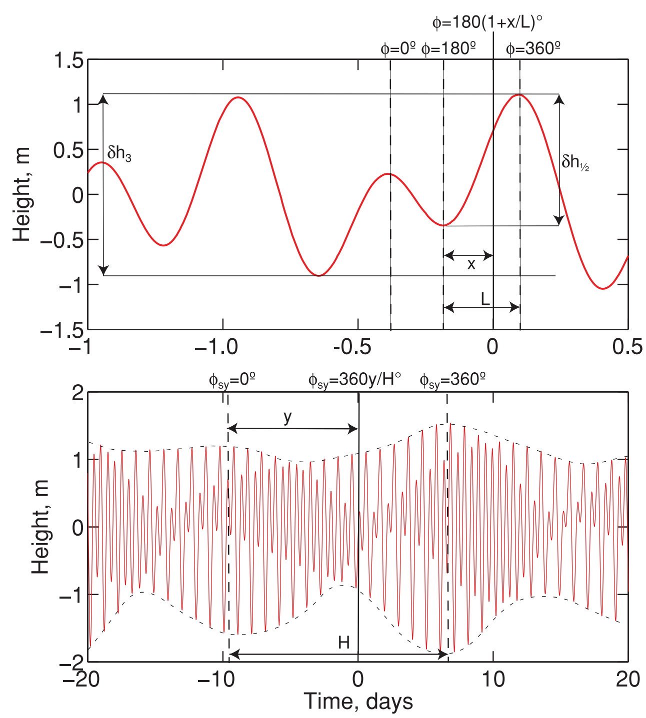

Figure 7. Sketch illustrating the method used to estimate various tidal parameters for an earthquake. (a) The tidal phase of an earthquake, ϕ occurring at time 0 days is determined by a linear interpolation between a phase of 0°/360° at high tide and a phase of 180° at low tide. The term $\delta h_{1/2}$ is the amplitude of the half cycle in which the earthquake occurs and δh_3 is the maximum range of the tides over three cycles ending at the tidal extreme following the earthquake. (b) The phase of the earthquake during the fortnightly peaks in tidal ranges near syzygy, ϕ_{sy} is defined by a linear interpolation between values of 0° and 360° at these peaks.

57 per cent of the time. To account for this bias, I adjust the earthquake counts in the phase histograms by a factor C

$$C = \frac{\bar{f}}{0.5}, \qquad \phi < 180^\circ$$
$$C = \frac{(1-\bar{f})}{0.5}, \quad \phi \geq 180^\circ, \tag{8}$$

where $\bar{f}$ is the mean fraction of time the tides are increasing at all earthquake locations in the data set being analysed. I also modify the Schuster test to account for this bias by redefining R

$$R^2 = \left(\sum_1^{N_{\text{tot}}} \cos\phi\right)^2 + \left(\sum_1^{N_{\text{tot}}} C\sin\phi\right)^2. \tag{9}$$

One limitation of the Schuster test is that it will not detect all non-random distributions. For example if the incidence of earthquakes increases equally at both low and high tides there will be no effect on R. Another way to test for non-random distributions is to count the number of earthquakes within particular phase limits and use a single-sided binomial test (e.g. Wonnacott & Wonnacott 1977) to calculate the probability of observing at least this many in a random population. I do this for the number of earthquakes with phases in the low tide half cycle ($90^\circ \leq \phi < 270^\circ$) and within 15° of low tide ($165^\circ \leq \phi < 195^\circ$).

The use of tidal phase in earthquake triggering studies does not take into account the tidal amplitude, which other studies have shown to be important (Wilcock 2001; Cochran *et al.* 2004). Many tidal cycles have small amplitudes and yet earthquakes occurring during such intervals are given equal significance to those during cycles with large amplitudes. One way to consider tidal height is to calculate the mean tidal height at the time of an earthquake; in the absence of tidal triggering the expected value is zero. I also consider the distribution of tide heights at the earthquake location and define a height percentile as the percentage of time the tide is lower than that at the time of the earthquake. For a random population the height percentiles should be uniformly distributed. I use a one-sided binomial test to search for statistically significant increases in the number of earthquakes below the 10th and 50th percentiles.

If the triggering of an earthquake is slightly delayed, then there may be an increased incidence of earthquakes during intervals when the tidal range is large. To search for this, I consider two quantities, the tidal range in the half cycle in which the earthquake occurs, $\delta h_{1/2}$ and the tidal range during the three cycles before the earthquake, δh_3 (Fig. 7a). This second measure accounts for the fact that semi-diurnal tides often include alternating low- and high-amplitude cycles and that an earthquake in a low-amplitude cycle or at the start of a high-amplitude cycle could be triggered by the preceding high-amplitude cycle. For both $\delta h_{1/2}$ and δh_3, I look at the time-weighted distribution of the values over a 1-yr interval centred on each earthquake and determine the percentage of the time, the values is lower than at the time of the earthquake. I use a binomial test to determine whether the number of earthquakes above the 50th percentile is significant.

I also search for an increased incidence of earthquakes near the fortnightly peaks in the tidal envelope (i.e. spring tides) that occur near syzygy (Hartzell & Heaton 1989; Kennedy *et al.* 2004). The instantaneous amplitude a of the tide is written (e.g. Bracewell 1978)

$$a^2(t) = h(t)^2 + H[h(t)]^2, \tag{10}$$

where H is the Hilbert transform. I define the fortnightly peaks in the tidal ranges by searching for times at which a exceeds all values within a 14-d window centred about that time (Fig. 7b). I use linear interpolation to define the phase of the earthquake within the fortnightly cycle, ϕ_{sy} (Fig. 7b). I apply a Schuster test to search for a non-random distribution and a binomial test to search for an increased incidence during intervals of larger tidal ranges ($\phi_{sy} \leq 90^\circ$ and $\phi_{sy} > 270^\circ$).

Since the catalogues I consider are not complete down to their minimum earthquake magnitude, it is possible that the statistical tests may be influenced by annual, seasonal and daily biases (Fig. 4). In order to account for such biases, I also determine alternate probabilities using Monte Carlo simulations. For each catalogue I assume that the probability of an earthquake at a particular time was proportional to the number of earthquakes in the catalogue during the year-month of the earthquake multiplied by the number of earthquakes in the whole catalogue during the same hour of the day. I assume that the earthquake locations remain unchanged and conduct 10000 simulations in which the time of each earthquake is assigned randomly using the temporal probabilities described above. I then determine the fraction of the simulations that satisfy each of the tidal triggering tests. In this way, I compute probabilities that were equivalent to each Schuster and binomial test and also assess whether the mean tidal height at the times of earthquakes deviates significantly from zero.

RESULTS

Fig. 8 shows histograms of the distribution of earthquake tidal phase and syzygy phase for the three data sets. The most prominent feature is a pronounced increase in earthquakes in the 'JdF/QCF' data set at low tide ($\phi = 180^\circ$ in Fig. 8a) and a decrease towards high tide. The 'A/AI' data set also appears to show higher earthquake counts near low tide (Fig. 8c). The histograms for syzygy phase (Figs 8d–f) do not show a clear increase in earthquakes near peak spring tides ($\phi_{\text{sy}} = 0^\circ$ and 360°).

Fig. 9 shows histograms of earthquake height percentiles, $\delta h_{1/2}$ and δh_3 for the three data sets. In the 'JdF/QCF' and 'A/AI' data sets there appears to be a tendency for the number of earthquakes to decrease with increasing height percentile but the trends are subtle. The histograms of $\delta h_{1/2}$ and δh_3 show no clear evidence for increased earthquake evidence during periods when the tidal cycles have large amplitudes (i.e. at high percentiles).

Table 3 summarizes the results of the statistical tests while Fig. 10 shows examples of the application of the Monte Carlo simulations to determining probabilities. In general the Monte Carlo simulations yield probabilities that are in good agreement with the Schuster and binomial tests indicating that the temporal biases in the catalogues do not significantly impact most tests. The most notable exception is the test of the number of earthquakes below the 10th height percentile for the 'A/AI' data set. The binomial test gives a probability of 0.243 of there being at the least the observed number of while the Monte Carlo simulations give a probability of 0.641. This discrepancy is the result of the uneven distribution with time of earthquakes in the 'A/AI' data set (Fig. 4c) that has resulted from the expanded monitoring of Alaskan volcanoes (Brantley *et al.* 2004) and variations in the amplitude of peak spring tides in the western Aleutians that occur on an 18.6-yr cycle. The large number of earthquakes in the last few years of the catalogue coincides with a period of spring tides with amplitudes larger than the long-term average. The Monte Carlo simulations account for the increased incidence of earthquakes in the lowest (and highest) height percentiles that would be expected from the recent increase in the rate of catalogued earthquakes. However, the

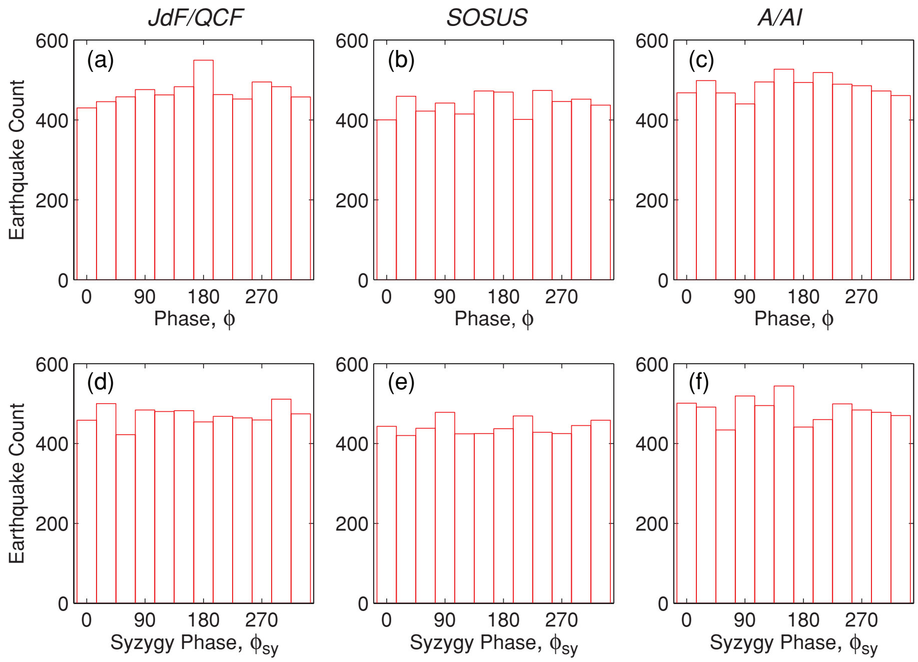

Figure 8. (a) Histogram showing the distribution of earthquake tidal phases for the 'JdF/QCF' data set. (b) and (c) As for (a) except for the 'SOSUS' and 'A/AI' data sets, respectively. (d)–(f) As for (a)–(c) except the histograms are for the phase of the earthquake within the fortnightly variations in tidal range.

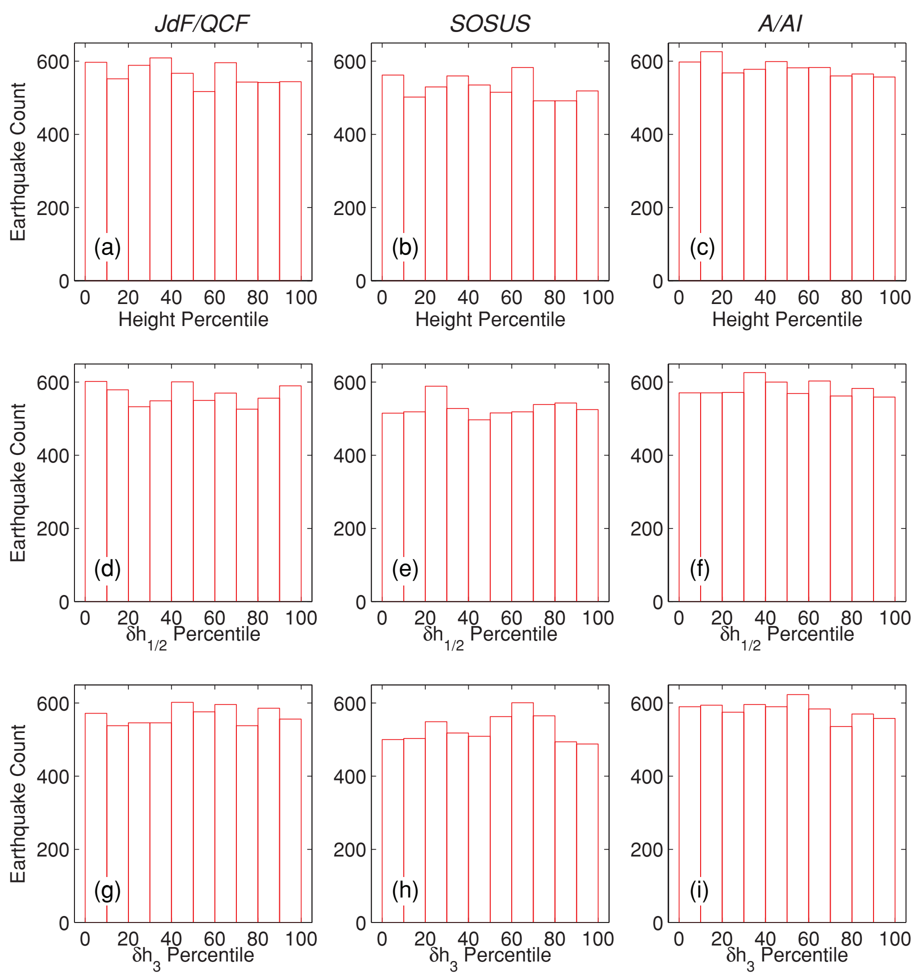

Figure 9. (a) Histogram of the tidal height percentile for the 'JdF/QCF' land-based data set. (b) and (c) As for (a) except for the 'SOSUS' and 'A/AI' data sets, respectively. (d)–(f) As for (a)–(c) except the histograms are for the $\delta h_{1/2}$ percentile. (g)–(i) As for (a)–(c) except the histograms are for the δh_3 percentile.

Table 3. Results of tidal triggering analysis.

	JdF/QCF	SOSUS	A/AI	A/AI subset	Combined
N_{tot}	5656	5290	5816	2000	11472
Tide phase					
Schuster test					
P_s	$\underline{0.020}$	0.387	0.120	0.394	$\underline{0.0028}$
$P_{\mathrm{mc}}(R^2 \geq R^2_{\mathrm{obs}})$	$\underline{0.019}$	0.385	0.129	0.392	$\underline{0.0026}$
Low-tide half cycle					
$N_{1,\mathrm{obs}} = \sum[(\phi > 90) \wedge (\phi < 270)]$	2909 (0.514)	2682 (0.507)	2973 (0.511)	1001 (0.501)	5882 (0.513)
$P_b(N_1 \geq N_{1,\mathrm{obs}})$	$\underline{0.016}$	0.158	$\underline{0.045}$	0.491	$\underline{0.0033}$
$P_{\mathrm{mc}}(N_1 \geq N_{1,\mathrm{obs}})$	$\underline{0.017}$	0.176	$\underline{0.045}$	0.463	$\underline{0.0027}$
Within 15° of low tide					
$N_{2,\mathrm{obs}} = \sum[(\phi > 165) \wedge (\phi < 195)]$	550 (0.097)	470 (0.089)	494 (0.085)	189 (0.095)	1044 (0.091)
$P_b(N_2 \geq N_{2,\mathrm{obs}})$	$\underline{0.0001}$	0.078	0.336	$\underline{0.040}$	$\underline{0.0017}$
$P_{\mathrm{mc}}(N_2 \geq N_{2,\mathrm{obs}})$	$\underline{0.0000}$	0.085	0.332	$\underline{0.038}$	$\underline{0.0017}$
Tide height					
Mean height					
$\bar{h}_{q,\mathrm{obs}}$ (cm)	−2.1	−1.1	−1.7	−3.5	−1.9
$P_{\mathrm{mc}}(\bar{h}_q \leq \bar{h}_{q,\mathrm{obs}})$	$\underline{0.020}$	0.138	$\underline{0.026}$	$\underline{0.026}$	$\underline{0.0016}$
Below 50th height percentile					
$N_{3,\mathrm{obs}} = \sum(h_q < h_{50})$	2914 (0.515)	2689 (0.508)	2969 (0.511)	1032 (0.516)	5883 (0.513)
$P_b(N_3 \geq N_{3,\mathrm{obs}})$	$\underline{0.011}$	0.116	0.056	0.079	$\underline{0.0031}$
$P_{\mathrm{mc}}(N_3 \geq N_{3,\mathrm{obs}})$	$\underline{0.011}$	0.159	$\underline{0.022}$	0.061	$\underline{0.0004}$
Below 10th height percentile					
$N_{4,\mathrm{obs}} = \sum(h_q < h_{10})$	597 (0.106)	562 (0.106)	598 (0.103)	225 (0.113)	1195 (0.104)
$P_b(N_4 \geq N_{4,\mathrm{obs}})$	0.086	0.069	0.243	$\underline{0.036}$	0.071
$P_{\mathrm{mc}}(N_4 \geq N_{4,\mathrm{obs}})$	0.093	$\underline{0.045}$	0.641	$\underline{0.030}$	0.196
Intervals with higher amplitude tides					
Tidal range of half cycle including earthquake					
$N_{5,\mathrm{obs}} = \sum(\delta h_{1/2} > \delta h_{1/2,50})$	2792 (0.494)	2642 (0.499)	2876 (0.495)	997 (0.499)	5668 (0.494)
$P_b(N_5 \geq N_{5,\mathrm{obs}})$	0.834	0.538	0.803	0.562	0.900
$P_{\mathrm{mc}}(N_5 \geq N_{5,\mathrm{obs}})$	0.831	0.572	0.779	0.610	0.892
Tidal range of three cycles preceding earthquake					
$N_{6,\mathrm{obs}} = \sum(\delta h_3 > \delta h_{3,50})$	2852 (0.504)	2711 (0.513)	2871 (0.494)	981 (0.491)	5723 (0.499)
$P_b(N_6 \geq N_{6,\mathrm{obs}})$	0.266	$\underline{0.036}$	0.837	0.808	0.600
$P_{\mathrm{mc}}(N_6 \geq N_{6,\mathrm{obs}})$	0.341	$\underline{0.050}$	0.888	0.850	0.730
Syzygy phase					
Schuster test					
P_s	0.800	0.946	0.670	0.717	0.982
$P_{\mathrm{mc}}(R^2_{sy} \geq R^2_{sy,\mathrm{obs}})$	0.801	0.945	0.682	0.720	0.939
Larger tidal ranges					
$N_{7,\mathrm{obs}} = \sum[(\phi_{sy} < 90°) \vee (\phi_{sy} > 270°)]$	2849 (0.504)	2686 (0.508)	2873 (0.494)	994 (0.497)	5722 (0.499)
$P_b(N_7 \geq N_{7,\mathrm{obs}})$	0.284	0.127	0.817	0.597	0.600
$P_{\mathrm{mc}}(N_7 \geq N_{7,\mathrm{obs}})$	0.286	0.131	0.824	0.694	0.615

Notes: Notation is as listed in the notation section and values in parentheses are the fraction of events satisfying the listed criteria. Underlined probabilities indicate correlations that are significant at a 95 per cent confidence level (i.e. the probabilities are ≤0.05).

Monte Carlo simulation will not account for any effects that result from a change in the spatial distribution of the earthquakes that accompanies the expansion of the network.

As can be inferred from inspecting the histograms (Figs 8d–f and 9d–i), the statistical tests show no convincing evidence for increased incidence of earthquakes during intervals of high tidal amplitudes. Only one of twelve tests applied to $\delta h_{1/2}$, δh_3 and ϕ_{sy} for the three data sets is significant at a 95 per cent confidence level; this is not unexpected for multiple tests of a random process (e.g. Emter 1997).

In contrast, all three data sets show evidence for increased earthquake incidence near low tides. The evidence for tidal triggering is particularly compelling for the 'JdF/QCF' data set. The Schuster test for tidal phase, the number of earthquakes in low-tide half cycles ($90° < \phi < 270°$), the mean earthquake tide height, and the number of earthquakes below the 50th height percentile are all significant at about a 98 per cent confidence level. The incidence of earthquake within 15° of low tide is 15 per cent higher than the average values and is significant at a very high confidence level.

The results for the 'SOSUS' data sets are less equivocal. The Shuster test does not detect a non-random phase distribution. The number of earthquakes with phases in the low-tide half cycles and within 15° of low tide, the mean earthquake tide height, and the number of earthquakes below the 10th and 50th height percentile all have probabilities below 0.2 but only the number of earthquakes below 10th height percentile is significant at a 95 per cent confidence level and only for the Monte Carlo simulation.

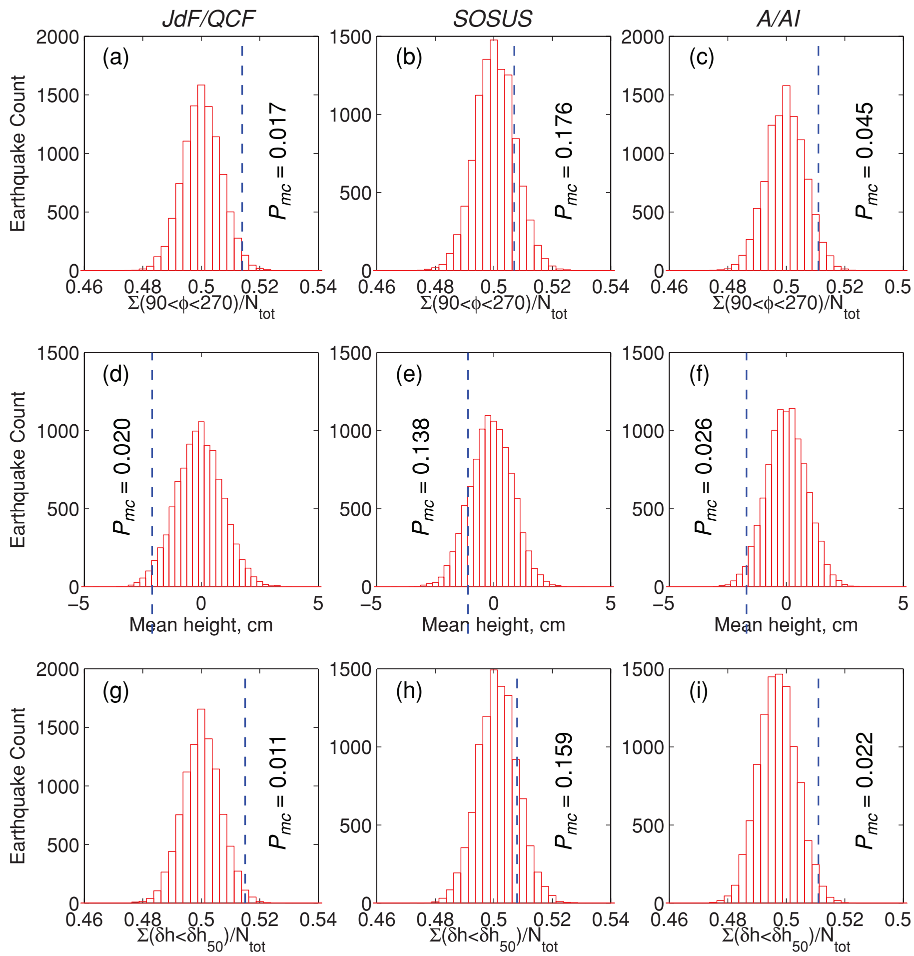

Figure 10. Examples of the Monte Carlo simulations. (a) Histogram plot of the distribution of the number of earthquakes during periods with a tide phase in the low-tide half for 10 000 simulations of the 'JdF/QCF' data set together with the observed value (blue dashed line). The Monte Carlo simulations are used to estimate the probability, P_{mc} of a number equal to or above the observed value assuming a random population of earthquakes. (b) and (c) As for (a) except for the 'SOSUS' and 'A/AI' data sets, respectively. (d)–(f) As for (a)–(c) except the histogram shows the mean tide height at the times of the and the probabilities are those of observing equal or lower values than are observed. (g)–(i) As for (a)–(c) except the histogram is for the number of earthquakes with a tide height percentile that exceeds 50 per cent and the probabilities are those of observing an equal or higher values than are observed.

For the 'A/AI' data set, the number of earthquakes in the low-tide half cycle and below the 50th height percentile, and the mean tidal height are all significant at a 95 per cent confidence level. However, the Schuster test for tidal phase and the number of earthquakes within 15° of low tide and below the 10th height percentile are not statistically distinguishable from random distributions.

A limitation of the 'A/AI' data set is that the western Aleutians have lower tidal ranges than other regions considered in this study. Thus, the solid earth tides represent a larger component of the total tidal stresses and the phase of the tidal stresses can deviate from that of the ocean tides (Fig. 6d). For this reason I also analysed a subset of the 'A/AI' data set comprising all earthquakes from regions with an rms tide height exceeding 0.65 m (Fig. 2). Unlike the full data set, the 'A/AI' subset shows no increase in earthquakes in low-tide half cycles but the earthquake incidence within 15° of low tide is 13 per cent above average values (Fig. 11a) and is significant at the 95 per cent confidence level. The numbers of earthquakes below the 10th and 50th height percentile (Fig. 11b) are significantly greater than expected at 95 and 90 per cent confidence levels, respectively.

Because the 'JdF/QCF' and 'A/AI' data sets are for the same time interval and were constructed with the same methodology, I also apply the statistical tests to this combined data set. Of the six tests for tidal phase and height only the number of earthquakes below the 50th height percentile is not significant at the 95 per cent confidence level.

DISCUSSION

This study reveals clear evidence for a small increase in the rates of seismicity at low tides in regional data sets of offshore earthquakes in the Northeast Pacific Ocean. In Table 3, I analyse three data sets, a subset of one, a combination of two and apply in total 30 statistical tests to search for a non-random distribution of earthquake tidal phases, mean earthquake tide heights that are significantly below zero, and increased incidences of earthquakes when the tidal phase and height corresponds to low tide. All but one of these tests suggest that the probability of achieving the observed distribution is <0.5 for a random distribution of earthquakes; the one exception is for a test of the number of earthquakes below the 10th height percentile in the 'A/AI' data set where the predictions of the binomial and Monte Carlo simulations disagree (see discussion in previous discussion). A total of 17 of the 30 tests are significant at the 95 per cent confidence level as determined by the Monte Carlo simulations.

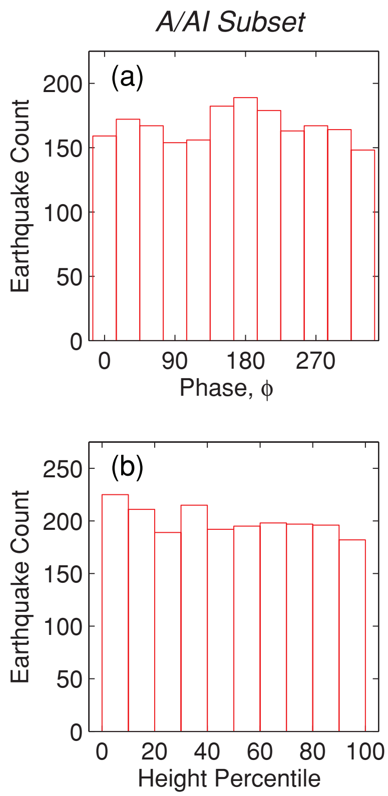

Figure 11. (a) Histogram showing the distribution of earthquake tidal phases for the subset of 'A/AI' data set with epicentres where the rms tidal amplitude exceeds 0.65 m. (b) Histogram of the tidal height percentile for the 'A/AI' subset.

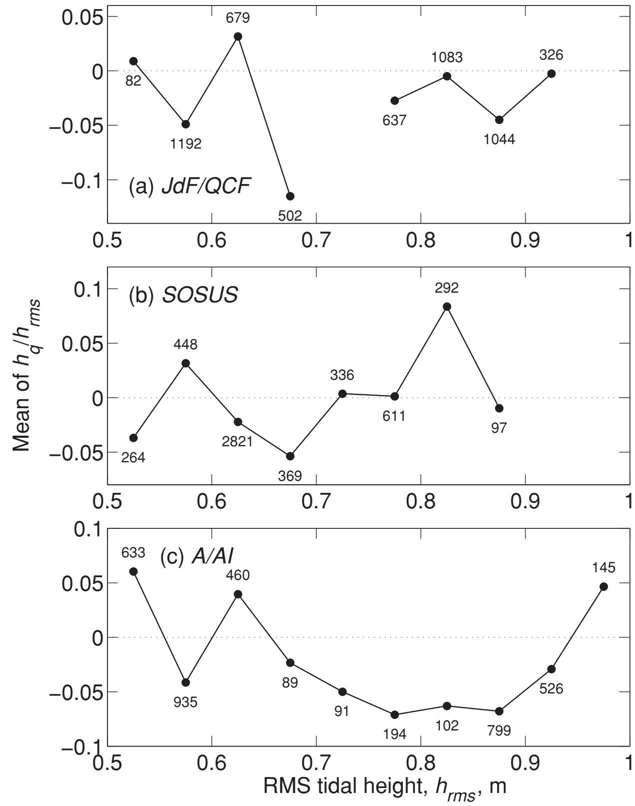

Figure 12. (a) Mean values of tide heights at the times of the earthquakes normalized to the rms tidal amplitude plotted against the rms tidal amplitude for the 'JdF/QCF' data set. Each mean is obtained by averaging earthquakes from locations where the rms tidal values falls in an 0.05-m-wide bin. Numbers next to each average are the number of earthquakes used to obtain the average; averages are not plotted if this is less than 50. (b) and (c) As for (a) except for the 'SOSUS' and 'A/AI' data sets, respectively.

The tidal triggering signal is strongest in the 'JdF/QCF' data set and weakest in the 'SOSUS' data set even though the two data sets come from the same region. As noted above the two data sets have only 208 events in common and the spatial distribution of earthquakes is significantly different (Fig. 1 and Table 2). However, from an inspection of the mean tide heights of earthquakes in different regions (Table 2), it is not clear that the difference in strength of the tidal triggering signal can be simply explained by differences in the spatial distribution of earthquakes. For example, the 'SOSUS' data set has a much higher proportion of earthquakes on the Blanco transform fault so the tidal triggering signal would be weaker in this data set if earthquakes from the Blanco were not affected by tidal triggering. However, inspection of Table 2 shows that for both the 'JdF/QCF' and 'SOSUS' data sets, the earthquakes on the Blanco Transform have a lower mean tide height than for the full data sets, which suggests that they are more affected by tidal triggering than the data sets as a whole. The 'SOSUS' catalogue also includes a higher proportion of mid-ocean ridge events, which other studies show to be strongly influenced by tidal triggering (Wilcock 2001; Tolstoy *et al.* 2002; Stroup *et al.* 2007).

The earthquakes in the 'SOSUS' data set tend to be further south and as a result the average tidal range is significantly lower in the 'SOSUS' data set than in the 'JdF/QCF' data set (Table 1). However, plots of the normalized mean earthquake tide height for different tide ranges (Figs 12a and b) for these two data sets show no clear trend that would demonstrate that the tidal triggering signal increases with tidal range. The generation of T-phases is likely strongest for earthquakes near the seafloor (e.g. de Groot-Hedin & Orcutt 2001) and so the 'SOSUS' data set may be biased towards shallower focal depths. Since the tidal stress fluctuations will be a larger proportion of the total stress at shallower depths, one might expect the tidal triggering signal to be stronger in the 'SOSUS' data set, which is the opposite of what is observed.

It should be noted that the 'SOSUS' data set is complicated by the presence of a significant number of gaps that resulted from interruptions in the data stream (Robert Dziak, personal communication 2008). The declustered 'SOSUS' data set comprises 5260 earthquakes and includes 8 intervals of >14 d without earthquakes. For the same time range the 'JdF/QCF' data set includes only 2011 earthquakes but there are no intervals of >14 days without earthquakes. I have not accounted for gaps in the catalogue in my Monte Carlo simulations and it is possible that if they are not randomly distributed they may have impacted the analysis of the 'SOSUS' data set.

The 'A/AI' data set shows a tidal triggering signal that is intermediate between the 'JdF/QCF' and 'SOSUS' data sets. In the Aleutians that tidal ranges are smaller and the phase of ocean tide phases may differ significantly from that of tidal stresses (Fig. 6d). This offset in phase may explain why the full data set shows no significant increase in the number of earthquakes within 15° of the low tide while the subset of data that excludes the Aleutians does. Excluding earthquakes in the Aleutians creates a data set with substantially higher average tidal ranges. The apparent strength of the tidal triggering signal in the 'A/AI' subset is stronger than in the full data set but its statistical significance is about the same because of the reduced number of events.

Unlike the other two data sets, the plot of normalized mean earthquake tide height against rms tide height for the 'A/AI' data set (Fig. 12c) shows a clear pattern. For the very highest tidal ranges (0.95–1 m), which occur south of Cook Inlet and Shelikof Strait (Fig. 2), the mean earthquake tide height is positive. Since the focal mechanisms of shallower offshore earthquakes in this region tend to have thrust mechanisms (e.g. Doser *et al.* 1999) that should always be favoured by low tide (Fig. 5), it seems unlikely that this can be attributed to the style of faulting in the region. It is most likely a result of the small number of earthquakes involved. The mean earthquake tide heights for rms tidal ranges between 0.65 and 0.95 m are consistently negative, while there is no consistent signal at lower tidal amplitudes.

Cochran *et al.* (2004) define the percentage of excess events, e, during periods of encouraging tidal stress as

$$e = 100\frac{N_{\mathrm{enc}} - (N_{\mathrm{tot}}/2)}{N_{\mathrm{tot}}}, \tag{11}$$

where N_{enc} is the number of encouraging events and the expression requires encouraging conditions to occur half the time. For my study, the observed excess event counts for favourable tidal phases ($N_{\mathrm{enc}} = N_1$ in Table 3) are 1.4 ± 0.7 and 1.1 ± 0.7 per cent for the 'JdF/QCF' and 'A/AI' data sets, respectively. For the tidal height ($N_{\mathrm{enc}} = N_3$ in Table 3) the equivalent values are 1.5 ± 0.7 and 1.0 ± 0.7 per cent. The uncertainties are determined using binomial probability distribution for the catalogue sizes (Vidale *et al.* 1998). When comparing my results to other studies it is important to note that the percentage of excess events as defined by eq. (11) is about factor of 4 smaller than the estimated increase in the rate of seismicity as defined by Vidale *et al.* (1998).

As noted above a number of studies of local earthquakes have reported high levels of tidal triggering on mid-ocean ridges (Wilcock 2001; Tolstoy *et al.* 2002; Stroup *et al.* 2007) including two studies on the Juan de Fuca Ridge (Wilcock 2001; Tolstoy *et al.* 2002). The levels of seismicity in these data sets increase by factors between about 2 and 5 when the stresses are most favourable, which is a much stronger tidal triggering signal than observed in the regional data sets considered in this paper. The levels of triggering at mid-ocean ridges may be influenced by stress amplification around magma bodies (Tolstoy *et al.* 2002) and by the high values of tidal stress perturbations relative to total stress at shallow depths. Tidal triggering was particularly strong on the East Pacific Rise prior to a volcanic eruption, an effect that has been attributed to high stressing rates maintaining stresses close to the critical threshold for failure in the lead up to an eruption (Stroup *et al.* 2007).

The data sets considered in this study include relatively few mid-ocean ridge earthquakes (18 per cent in 'SOSUS', 4 per cent in 'JdF/QCF'). The detection threshold on the Juan de Fuca and Gorda Ridges is too low in the 'JdF/QCF' data set to detect most ridge earthquakes and in the 'SOSUS' data set, the declustering algorithm will reduce the volcanic swarms that may be most prone to triggering (Stroup *et al.* 2007) to a single event.

The tidal triggering signal in the regional data sets I analyse is also much weaker than observed in some subduction zones prior to large earthquakes (Tanaka *et al.* 2002b; Tanaka *et al.* 2006). In these studies the high levels of tidal triggering were also attributed to stress states reaching a near critical level prior to large earthquakes.

Cochran *et al.* (2004) use global thrust and California strike-slip earthquakes to determine a relationship between the percentage of excess events and the peak tidal coulomb stress. For a coefficient of friction $\mu = 0.4$ (the value assumed by Cochran *et al.* (2004)) and a Poisson's ratio $\nu = 0.28$, the mean value of the coulomb stress predicted by eqs (3) and (4) for a randomly distributed population of faults is

$$\bar{\sigma}_c = -0.23\,\sigma_{zz}. \tag{12}$$

For the 'JdF/QCF' and 'A/AI' data sets the mean tidal ranges are 3.56 and 3.06 m, respectively (Table 1). Thus, peak Coulomb stresses will correspond unloading about 1.5 m of water. Using eqs (1) and (11) with $h = -1.5$ m, $\rho = 1030$ kg m^{-3} and $g = 9.8$ m s^{-2}, I estimate an average peak Coulomb stress of 0.004 MPa. For this stress, Cochran *et al.* (2004) predict an excess event percentage, $e = 3$ per cent (see their Fig. 4) based on a least squares fit to their data assuming both rate- and state-dependent friction and stress corrosion models. Thus, the strength of the tidal triggering signal in my data sets appears weaker than predicted by Cochran *et al.* (2004). However, the observations on which their predictions are based have considerable uncertainty. Moreover, favourable tidal stresses will not always coincide with low tides because of the effects of fault orientation (Fig. 5) and solid earth tides (Fig. 6), and so my study will likely underestimate the percentage of excess events during intervals of actual favourable stress.

Based on laboratory experiments, Beeler & Lockner (2003) estimate the number of earthquakes necessary to detect a correlation using the Schuster test as

$$N_{\mathrm{tot}} \approx \frac{-\ln(P_S)}{(\Delta\sigma_c/2a\sigma_n)^2}, \tag{13}$$

where P_S is the desired Schuster probability, $\Delta\sigma_c$ is the amplitude of the tidal Coulomb stress, σ_n is the total normal stress across the fault and a is a constant that was experimentally determined by Beeler & Lockner (2003) to be 0.0045 ± 0.002. Using $P_S = 0.05$; $\Delta\sigma_c = 0.004$ MPa and $\sigma_n = 90$ MPa (a normal stress that is appropriate for a depth 5 km depth below the seafloor assuming hydrostatic fluid pressures), yields $N_{\mathrm{tot}} = 38000$–260000 for the range of a values. Given that the 'JdF/QCF' and 'A/AI' both contain only 5000–6000 earthquakes and show evidence for tidal triggering (Table 3), my results suggest either that the tidal triggering signal is stronger than predicted by Beeler & Lockner or that the fluids on the faults are commonly at pressures well above hydrostatic.

CONCLUSIONS

In this paper, I present a systematic investigation for a correlation between earthquake tide height and the rates of seismicity in the Northeast Pacific Ocean using three declustered regional earthquake catalogues. The primary conclusions of this study are:

(1) There is no evidence for an increase in seismicity during intervals of large tidal range but there is clear evidence for small but significant increase in earthquake rates near low tide.

(2) The tidal triggering signal is particularly clear in land based catalogues for the Juan de Fuca Plate and Queen Charlotte Fault region where there is a 15 per cent increase in seismicity within 15° of low tide that is statistically significant to a very high level of confidence.

(3) The increased rates of seismicity I observe are reasonably consistent with predictions based on an earlier analysis of thrust earthquake in the global Harvard CMT catalogue (Cochran *et al.* 2004) and stronger than predicted by laboratory simulations of fault failure under tidal loading (Lockner & Beeler 1999; Beeler & Lockner 2003).

ACKNOWLEDGMENTS

I thank Robert Dziak and Kelin Wang for useful discussions, John Cassidy for assistance obtaining data from the Canadian National Earthquake Database and John Vidale and an anonymous referee for thorough reviews of an earlier version of this manuscript.

Notation used in the text.

a	Instantaneous tidal amplitude (m)
C	Factor to account for asymmetry of tides in phase data
E	Young's modulus (Pa)
e	Percentage of excess earthquakes during periods of encouraging stress
$\bar{f}$	Mean of the fraction of time the tides are increasing at each epicentre
h	Tide height (m)
h_{rms}	Root mean square tide height (m)
$\bar{h}_q$	Mean tidal height at times of earthquake (m)
h_{10}	The 10th percentile value of the tidal height at the earthquake location (m)
N_{enc}	Number of earthquakes during times of encouraging tidal stress
N_{tot}	Number of earthquakes in the data set
N_{reg}	Number of earthquakes in a region
N_{i}	Number of earthquakes satisfying the listed criteria
obs	Subscript to indicate an observed value
P_{S}	Probability determined from a Schuster test
P_{b}	Probability determined from a one-sided binomial test.
x	Distance offshore (km)
R	Vector sum of phasors
P_{mc}	Probability determined from a Monte Carlo simulation.
δ	Fault dip
λ	Fault rake
$\delta h_{1/2}$	Amplitude of the tidal half cycle that encloses an earthquake (m)
δh_3	Maximum range of the tides over three cycles before an earthquake (m)
$\delta h_{1/2,50}$	The 50th percentile value of $\delta h_{1/2}$ (m)
$\delta h_{3,50}$	The 50th percentile value of δh_3 (m)
ϕ	Earthquake tidal phase (°)
ϕ_{sy}	Earthquake phase within the fortnightly variation in tidal ranges (°)
$\Delta\sigma_{\mathrm{c}}$	Tidal Coulomb stress promoting failure on the fault plane (Pa)
$\Delta\sigma_{xx}$, $\Delta\sigma_{yy}$	Tidal horizontal principal stress (Pa)
$\Delta\sigma_n$	Tidal normal stress acting on the fault plane (Pa)
$\Delta\sigma_{zz}$	Tidal vertical stress (Pa)
$\Delta\varepsilon_{xx}$, $\Delta\varepsilon_{yy}$	Tidal horizontal normal strains
$\Delta\varepsilon_{xy}$	Tidal horizontal shear strain
σ_{xy}	Tidal horizontal shear stress
ρ	Seawater density (kg m^{-3})
τ	Shear stress acting on the fault plane in the direction of fault failure (Pa)
ν	Poisson's ratio
μ_{f}	Effective coefficient of friction
Σ	Sum of all the earthquakes satisfying the logical expression that follows
$\vee$	Logical 'or'
$\wedge$	Logical 'and'
A_{S}	Source pressure amplitude for earthquakes located with SOSUS (dB)
M	Earthquake magnitude

REFERENCES

Agnew, D.C., 1996. SPOTL: some programs for ocean-tide loading, in *SIO Ref. Ser. 96-8,* pp. 35, Scripps Inst. of Oceanogr., La Jolla, CA

Agnew, D.C., 1997. NLOADF: a program for computing ocean-tide loading, *J. geophys. Res.,* **102,** 5109–5110.

Beeler, N.M. & Lockner, D.A., 2003. Why earthquakes correlate weakly with the solid Earth tides: effects of periodic stress on the rate and probability of earthquake occurrence, *J. geophys. Res.,* **108,** doi:10.1029/2001JB001518.

Berg, E., 1966. Triggering of the Alaskan earthquake of March 28, 1964, and major aftershocks by low ocean tide loads, *Nature,* **210,** 893–896.

Bird, P., 1996. Computer simulations of Alaskan neotectonics, *Tectonics,* **15,** 225–236.

Bracewell, R.N., 1978. *The Fourier Transform and its Applications,* 2nd edn, McGraw-Hill, New York.

Brantley, S.R., McGimsey, R.G. & Neal, C.A., 2004. The Alaska Volcano Observatory-Expanded monitoring of volcanoes yields results, Survey, U. G., Fact Sheet 2004–3084.

Braunmiller, J. & Nábělek, J., 2002. Seismotectonics of the Explorer region, *J. geophys. Res.,* **107,** 2208, doi:2210.1029/2001JB000220.

Braunmiller, J. & Nábělek, J., 2008. Segmentation of the Blanco Transform Fault Zone from earthquake analysis: complex tectonics of an oceanic transform fault, *J. geophys. Res.,* **113,** B07108, doi:07110.01029/02007JB005213.

Cessaro, R.K. & Hussong, D.M., 1986. Transform seismicity at the intersection of the Oceanographer fracture zone and the Mid-Atlantic Ridge, *J. geophys. Res.,* **91,** 4839–4853.

Cochran, E.S., Vidale, J.E. & Tanaka, S., 2004. Earth tides can trigger shallow thrust fault earthquakes, *Science,* **306,** 1164–1166.

Coffin, M.F., Gahagan, L.M. & Lawver, L.A., 1998. Present-day plate boundary digital data compilation, University of Texas Institute for Geophysics Technical Report No. 174, pp. 5.

Cotton, L.A., 1922. Earthquake frequency with spatial reference to tidal stresses in the lithosphere, *Bull. seism. Soc. Am.,* **12,** 47–198.

Cowan, D.S., Botros, M. & Johnson, H.P., 1986. Bookshelf tectonics: rotated crustal blocks within the Sovanco fracture zone, *Geophys. Res. Lett.,* **13,** 995–998.

de Groot-Hedin, C.D. & Orcutt, J.A., 2001. Excitation of T-phases by seafloor scattering, *J. acoust. Soc. Am.,* **109,** 1944–1954.

Deng, J. & Sykes, L.R., 1997. Stress evolution in southern California and triggering of moderate-, small-, and micro-size earthquakes, *J. geophys. Res.,* **102,** 24 411–24 435.

Dieterich, J.H., 1987. Nucleation and triggering of earthquake slip: effect of periodic stress, *Tectonophysics,* **144,** 127–139.

Doser, D.I., Veilleux, A.M. & Velasquez, M., 1999. Seismicity of the Prince William Sound region for over thirty years following the 1964 Great Alaska earthquake, *Pure appl. Geophys.,* **154,** 593–632.

Egbert, G., Bennett, A. & Foreman, M., 1994. TOPEX/Poseidon tides estimated using a global inverse model, *J. geophys. Res.,* **99,** 24 821–24 852.

Egbert, G.D. & Erofeeva, S.Y., 2002. Efficient inverse modeling of barotropic ocean tides, *J. Atmos. Ocean. Technol.,* **19,** 183–204.

Emter, D., 1997. Tidal triggering of earthquakes and volcanic events, in *Tidal Phenomena,* pp. 293–309, eds Bhattacharji, S., Friedman, G., Neugebauer, H.J. & Seilacher, A., Springer, New York.

Fox, C.G., Dziak, R.P., Marumoto, H. & Schreiner, A.E., 1994. Potential for monitoring low-level seismicity on the Juan de Fuca Ridge using military hydrophone arrays, *Mar. Tech. Soc. J.,* **27,** 22–30.

Gross, S. & Bürgmann, R., 1998. Rate and state of background stress estimated from the aftershocks of the 1989 Loma Prieta, California, earthquake, *J. geophys. Res.,* **103,** 4915–4927.

Gross, S. & Kisslinger, C., 1997. Estimating tectonic stress rate and state with Landers aftershocks, *J. geophys. Res.,* **102,** 7603–7612.

Hartzell, S. & Heaton, T., 1989. The fortnightly tide and the tidal triggering of earthquakes, *Bull. seism. Soc. Am.,* **79,** 1282–1286.

Jaeger, J.C. & Cook, N.G.W., 1979. *Fundamentals of Rock Mechanics,* 3rd edn, Chapman and Hall, London.

Kagan, Y.Y. & Jackson, D.D., 1998. Spatial aftershock distribution: effect of normal stress, *J. geophys. Res.,* **103,** 24 453–24 467.

Kanamori, H. & Anderson, D.L., 1975. Theoretical basis of some empirical relations in seismology, *Bull. seism. Soc. Am.,* **65,** 1073–1095.

Kennedy, M., Vidale, J.E. & Parker, M.G., 2004. Earthquakes and the moon: syzygy predictions fail the test, *Seismol. Res. Lett.,* **75,** 607–612.

King, G.C.P., Stein, R.S. & Lin, J., 1994. Static stress changes and the triggering of earthquakes, *Bull. seism. Soc. Am.,* **84,** 935–953.

Klein, F.W., 1976. Earthquake swarms and the semidiurnal Solid Earth tide, *Geophys. J. R. astr. Soc.,* **45,** 245–295.

Knopoff, L., 1964. Earth tides as a triggering mechanism for earthquakes, *Bull. seism. Soc. Am.,* **54,** 1865–1870.

Kreemer, C., Govers, R., Furlong, K.P. & Holt, W.E., 1998. Plate boundary deformation between the Pacific and North America in the Explorer region, *Tectonophysics,* **293,** 225–238.

Lockner, D.A. & Beeler, N.M., 1999. Premonitory slip and tidal triggering of earthquakes, *J. geophys. Res.,* **104,** 20 133–20 151.

McNutt, S.R. & Beavan, R.J., 1981. Volcanic earthquakes at Pavlof Volcano correlated with the solid earth tide, *Nature,* **294,** 615–618.

Melchior, P., 1983. *The Tides of the Planet Earth,* 2nd edn, Pergamon, New York.

Métivier, L., de Viron, O., Conrad, C.P., Renault, S., Diament, M. & Patau, G., 2009. Evidence of earthquake triggering by solid earth tides, *Earth planet. Sci. Lett.,* **278,** 370–373.

Reasenberg, P., 1985. Second-order moment of Central California Seismicity, 1969–1982, *J. geophys. Res.,* **90,** 5479–5495.

Reasenberg, P.A. & Simpson, R.W., 1992. Response of regional seismicity to the static stress change produced by the Loma Prieta earthquake, *Science,* **255,** 1687–1690.

Ristau, J., Rogers, G.C. & Cassidy, J.F., 2003. Moment magnitude-local magnitude calibration for earthquakes off Canada's west coast, *Bull. seism. Soc. Am.,* **93,** 2296–2300.

Rowlett, H. & Forsyth, D.W., 1984. Recent faulting and microearthquakes at the intersection of the Vema Fracture Zone and the Mid-Atlantic Ridge, *J. geophys. Res.,* **89,** 6074–6094.

Scholtz, C.H., 2002. *The Mechanics of Earthquakes and Faulting,* 2nd edn, Cambridge University Press, Cambridge.

Schreiner, A.E., Fox, C.G. & Dziak, R.P., 1995. Spectra and magnitudes of T-waves from the 1993 earthquake swarm on the Juan de Fuca Ridge, *Geophys. Res. Lett.,* **22,** 139–142.

Shaw, P.R., 1994. Age variations of oceanic crust Poisson's ratio: inversion and a porosity evolution model, *J. geophys. Res.,* **99,** 3057–3066.

Stroup, D.F., Bohnenstiehl, D.R., Tolstoy, M., Waldhauser, F. & Weekly, R.T., 2007. Pulse of the seafloor: tidal triggering of microearthquakes at 9°50'N East Pacific Rise, *Geophys. Res. Lett.,* **34,** L15301, doi:15310.11029/12007GL030088.

Taber, J.J., Billington, S. & Engdahl, E.R., 1991. Seismicity of the Aleutian Arc, in *Neotectonics of North America,* pp. 29–46, eds Slemmons, D.B., Engdahl, E.R. & Zoback, M.D. & Blackwell, D.D., Geological Society of America, Boulder, Colorado.

Tanaka, S., Ohtake, M. & Sato, H., 2002a. Evidence for tidal triggering of earthquakes as revealed from statistical analysis of global data, *J. geophys. Res.,* **107,** 2211, doi:2210.1029/2001JB001577.

Tanaka, S., Ohtake, M. & Sato, H., 2002b. Spatio-temporal variation of the tidal triggering effect on earthquake occurrence associated with the 1982 South Tonga earthquake of Mw 7.5, *Geophys. Res. Lett.,* **29,** doi:10.1029/2002GL015386.

Tanaka, S., Sato, H., Matsumura, S. & Ohtake, M., 2006. Tidal triggering of earthquakes in the subducting Philippine Sea plate beneath the locked zone of the plate interface in the Tokai region, Japan, *Tectonophysics,* **417,** 69–80.

Tolstoy, M., Vernon, F.L., Orcutt, J.A. & Wyatt, F.K., 2002. Breathing of the seafloor: tidal correlations of seismicity at Axial Volcano, *Geology,* **30,** 503–506.

Tréhu, A.M., Braunmiller, J. & Nabelek, J., 2008. Probable low-angle thrust earthquakes on the Juan de Fuca-North American plate boundary, *Geology,* **36,** 127–130.

Tsuruoka, H., Ohtake, M. & Sato, H., 1995. Statistical test of the tidal triggering of earthquakes: contribution of the ocean tide loading effect, *Geophys. J. Int.,* **122,** 183–194.

Turcotte, D.L. & Schubert, G., 2002. *Geodynamics: Applications of Continuum Mechanics to Geological Problems,* 2nd edn, Cambridge University Press, New York, NY.

Vidale, J.E., Agnew, D.C., Johnston, M.J.S. & Oppenheimer, D.H., 1998. Absence of earthquake correlation with Earth tides: an indication of high preseismic fault stress rate, *J. geophys. Res.,* **103,** 24 567–24 572.

Wang, K. & He, J., 1999. Mechanics of low-stress forearcs: Nankai and Cascadia, *J. geophys. Res.,* **104,** 15 191–15205.

Wein, A.S. & Shearer, P.M., 2004. A comprehensive search for tidal triggering of Southern California earthquakes, *EOS. Trans. Am. geohhys. Un.,* **85,** Fall Meet. Suppl., Abstract S23A-0297.

Wilcock, W.S.D., 2001. Tidal triggering of microearthquakes on the Juan de Fuca Ridge, *Geophys. Res. Lett.,* **28,** 3999–4002.

Wonnacott, T.H. & Wonnacott, R.J., 1977. *Introductory Statistics,* Wiley, New York.